Research Article

Umar Nazir, Umair Khan*, Hamad Almujibah, and Hami Gündoğdu

Utilizing slip conditions on transport phenomena of heat energy with dust and tiny nanoparticles over a wedge

https://doi.org/10.1515/phys-2024-0106
received July 29, 2024; accepted November 29, 2024

Abstract: The present problem investigates 3D flow over an expanding wedge geometry of a tangent-hyperbolic Casson fluid. A two-phase approach considers a liquid phase and a dusty fluid, while a Darcy–Forchheimer law is used to model this fluid flow to capture motion and heat transfer. The several aspects are based on variable thermal radiation, heat sink effects, and slip conditions applied. A tri-hybrid nanofluid comprising silicon dioxide, copper, and aluminum oxide nanoparticles suspended in ethylene glycol, the base fluid, is incorporated into the analysis. The derivation of nonlinear ordinary differential equations (ODEs) is used to characterize momentum, thermal behavior, and fluid motion under these circumstances. ODEs are formulated using similarity transformations and slip conditions. The finite element approach is employed. It is estimated that the fluid phase on the heat transfer rate and skin friction coefficient is higher than the dusty phase on the Nusselt number and skin friction coefficient. The heat transfer rate for ternary hybrid nanofluid is larger than that for hybrid nanofluid.

Keywords: tri-hybrid nanofluid, magnetic field, slip conditions, dusty fluid, FEM

*** Corresponding author: Umair Khan,** Department of Mathematics, Faculty of Science, Sakarya University, Serdivan/Sakarya, 54050, Turkey; Department of Mathematics, Saveetha School of Engineering, Saveetha Institute of Medical and Technical Sciences, Saveetha University, Chennai, 602105, Tamil Nadu, India, e-mail: umairkhan@sakarya.edu.tr
Umar Nazir: Department of Mathematics, Faculty of Science, Khon Kaen University, Khon Kaen, 40002, Thailand
Hamad Almujibah: Department of Civil Engineering, College of Engineering, Taif University, P.O. Box 11099, Taif, 21974, Saudi Arabia
Hami Gündoğdu: Department of Mathematics, Faculty of Science, Sakarya University, Serdivan/Sakarya, 54050, Turkey

Nomenclature

B^*	pressure gradient number
B_0	magnetic induction number
BCs	boundary conditions
Cf_x, Cf_y	skin friction coefficient
c_p	specific heat capacitance
Ec	Eckert number
e	elements
Fr	Forchheimer number
F_s	Darcy's number
k^*	volume fraction
K^s	Inertia coefficient with porous medium
l_1, l_2	Ratios of surface velocity
M	Magnetic number
N	drag force
Nr	Radiation number
Nu	Nusselt number
n	power law index number
Pr	Prandtl number
Q	heat sink
Re	Reynolds number
$\partial_{\mathrm{Al_2O_3}}$, ∂_{Cu}, $\partial_{\mathrm{TiO_2}}$	volume fractions
T	temperature
T_p	temperature of dusty model
T_r	temperature ratio
T_∞	ambient temperature
thnf	tri-hybrid nanofluid
u_p, w_p, v_p	velocity components for dusty flow model
u_w	wall velocity
ν	kinematic viscosity
V, W, U	velocity components
We	Weissenberg number
y, x, z	Space coordinates
$\in$	Darcy's number
ρ_p	density for dusty model
λ_2, λ_1	multiple slip coefficients
β	Casson fluid number
σ	electrical conductivity

MHD	Magnetohydrodynamic
EG	Ethylene glycol
Γ^e	time relaxation number
ρ	density
η	independent variable
Θ	dimensionless temperature
γ	shear-to-strain rate number
OHAM	Optimal homotopy analysis method

1 Introduction

Complex non-Newtonian fluids are described by the tangent-hyperbolic Casson fluid model, which combines concepts from the Casson fluid model with tangent-hyperbolic shear-thinning behavior. The tangent hyperbolic model is called the shear thinning model. In such fluids, the shear rate is enhanced resulting in viscosity decreases. Non-Newtonian fluids with yield stress behavior are known as Casson fluids. Examples of the Casson fluid are blood, paints, chocolate, inks, creams and toothpaste, *etc.* Examples of hyperbolic tangent fluids are drilling muds, mayonnaise, ketchup, gels, paints and creams, *etc.* The applications of tangent-hyperbolic Casson fluid are utilized in polymer solutions, biological fluids, suspensions, the food industry, printing and industrial slurries, care products, and industrial processes. Bilal *et al.* [1] simulated the results of Casson fluid in heat transfer mechanism on a stretching surface utilizing Darcy's law. They have used heterogeneous and homogeneous reactants along with non-Fourier's theory. The analytical results were obtained utilizing homotopy approach. They have estimated that the heat energy was enhanced when the magnetic number was boosted. Sohail *et al.* [2] determined the numerical consequences in mass and heat transfer utilizing non-Fourier's approach in Casson fluid *via* Hall forces and ion slip currents. They estimated the Lorentz force and diffusion phenomenon. Malik *et al.* [3] experienced the Lorentz force of hyperbolic tangent liquid near a stretching

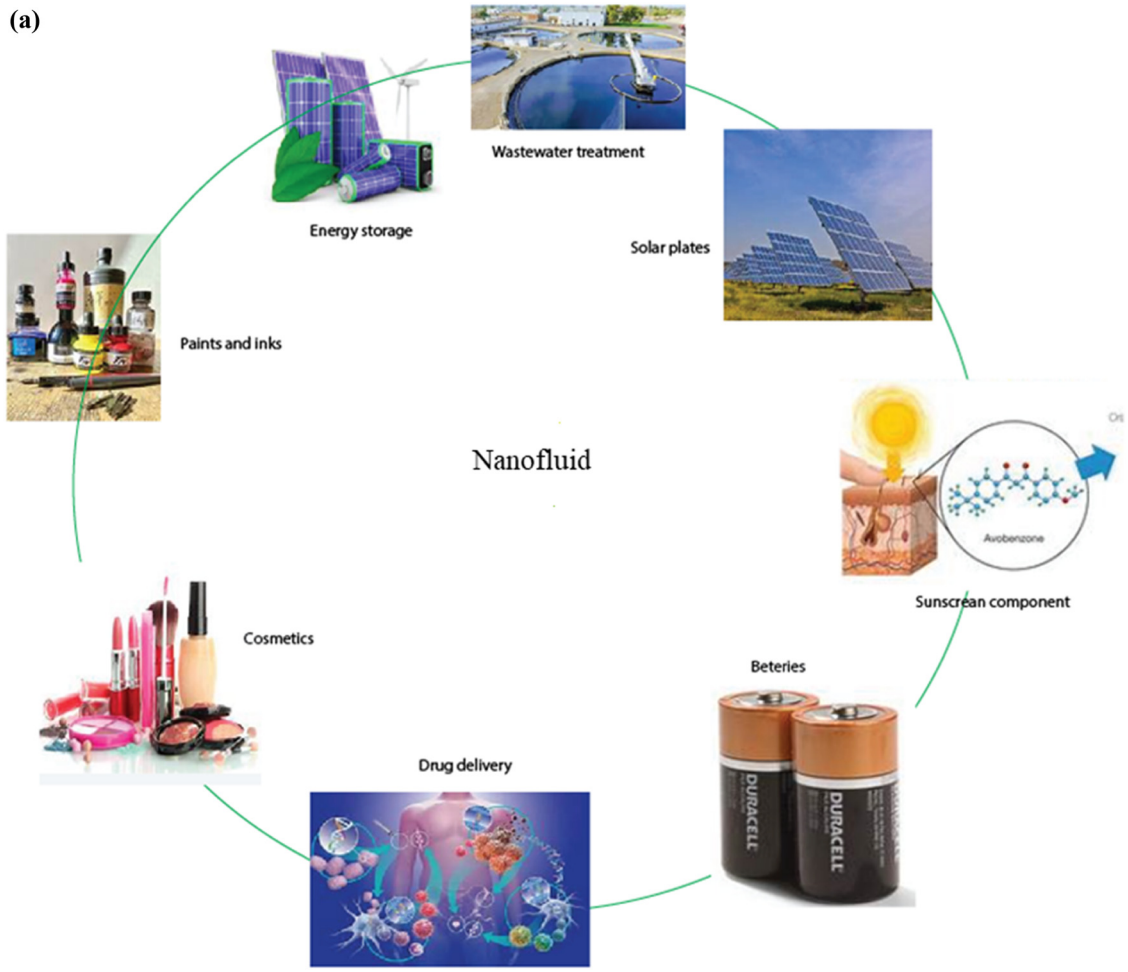

Figure 1: (a) Applications of nanofluid. (b) Flow chart of desired model and mixture of nanofluid. (c) Conversion of c-domain. (d) Elements related to sub-domain.

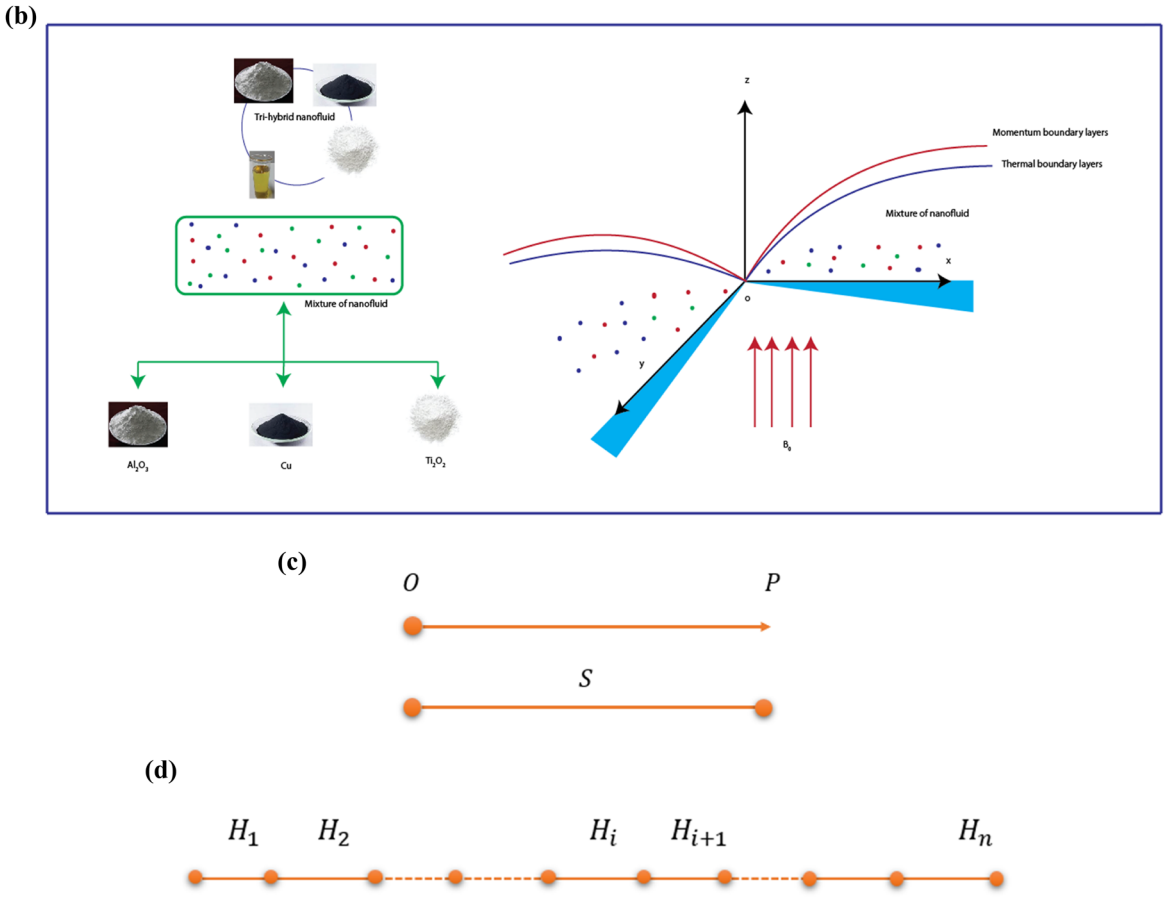

Figure 1: (*Continued*)

cylinder. They observed the model's numerical results using the Keller Box approach. Gaffar *et al.* [4] observed the mechanism of tangent hyperbolic rheology in heat energy transfer on a sphere *via* slip conditions. They have used the Keller Box approach for numerical purposes. Hayat *et al.* [5] utilized OHAM methodology to determine numerical outcomes of Prandtl fluid on the surface considering non-Fourier's law. They have investigated the concentration and temperature decrease as a function of the thermal and concentration relaxation parameters, respectively. Saleem *et al.* [6] studied the mechanism of mono and hybrid nanoparticles in Newtonian material on a shrinking plate. They have implemented thermal radiation and Eckert number using slip conditions. Keller Box approach has been used for numerical consequences. Temperature distribution increased when the Prandtl number was enhanced while the velocity field declined when the magnetic number was increased. Ramana *et al.* [7] determined the motion and heat energy of three-dimensional (3D) in Newtonian fluid considering Darcy's law. They estimated the rotating motion and heat sink utilizing the boundary value problem (bvp)5c approach. They estimated that Nusselt number increased when magnetic, radiation, and porosity numbers increased. Nisar *et al.* [8] discussed the phenomena of Bingham fluid adding the suspension of nanofluid considering thermal radiation, Brownian, and thermophoresis aspects. Further, they have considered viscous dissipation and thermal transport. Aziz *et al.* [9] assumed the mechanism of concentrated spoof surface (highly) considering LC-resonance law. Mishra and Pathak [10] experienced the influences of ternary and hybrid nano-structures in the heat transfer mechanism on a cylinder with heat absorption. According to the results, when the thermal radiation parameter and Eckert number increased, the ternary hybrid nanofluid's thermal profiles increased relative to that of the hybrid nanofluid. Govind *et al.* [11] estimated computational sequences of hybrid nanofluid in heat transfer mechanism on a flat plate considering the Lorentz force and Eckert number. The bvp4c technique is adopted for numerical purposes. Drag force accelerated as a result of an increase in magnetic parameter M, which raises entropy. Ali *et al.* [12] experienced Casson rheology by inserting a hybrid nanofluid toward an oscillating plate. They have considered the radiation mechanism, MHD, and gold nanoparticles. The numerical solutions of the problem have been determined by Laplace transform methodology. Hayat *et al.* [13] observed the role of 3D flow in nanofluid

considering Darcy's law and thermophoretic diffusion on a rotating surface. They used the OHAM approach for analytical outcomes. Ogunsola and Oyedotun [14] captured the consequences of Casson rheology in a channel considering hybrid nano-liquid. They considered thermal radiation and Eckert parameters for study flow and heat transfer mechanism. Paul *et al.* [15] experimented the numerical assessment of the Lorentz force toward a stretching cylinder containing nanofluid and tri-hybrid nanofluid. They determined the mechanism of mass transfer and heat energy rates using activation energy. Rehman *et al.* [16] found the mechanism of unsteady motion of Casson rheology including the Lorentz force. They adopted the HAM analysis approach for analytical results. They included that as values increase, velocity decreased, and a greater volume fraction of nanoparticles further reduces velocity. Soomro *et al.* [17] influenced the 2-dimensional mechanism of MHD Casson fluid including viscous dissipation *via* stability analysis. A mechanism of hybrid nanofluid has been observed *via* no-slip conditions. Ramasekhar *et al.* [18] discussed the computational study of Casson fluid in heat transfer by inserting hybrid nanofluid along with thermal radiation. They utilized heat transfer on the stretching plate. Skin friction and Nusselt number profiles were improved by increasing the Casson fluid and radiation parameters. Subhani *et al.* [19] explored the theory of the Lorentz force along with hybrid nanofluid in micropolar fluid with thermal radiation across expanding/stretching plates. They experienced the mechanism of entropy generation and numerically solved the model by bvp-4c approach. Aziz *et al.* [20] studied the impacts of Jeffrey liquid inserting the role of nanofluid along with activation energy on a rotating surface utilizing a thermophoretic mechanism. They adopted the OHAM approach for analytical works. Aziz *et al.* [21] experienced the influences of 3D swirling flow in mass diffusion and heat energy with Maxwell rheology. Thermal radiation and chemical mechanisms were implemented. The ND-Solve technique has been used for numerical purposes. Faltas and El-Sapa [22] addressed the micropolar fluid with change in electroosmotic motion and microrotation and periodic time. They solved pertinent parameters analytically. El-Sapa and Al-Hanaya [23] analyzed the effects of a couple of stress liquids in rotating spheres. They discussed the micropolar Eringen model for microstructure fluids and a linearized Poisson–Boltzmann equation serves as the study's foundations. Alotaibi and El-Sapa [24] visualized the role of the Lorentz force with liquid's density along with homogeneous and isotropic in couple stress and the body force acting in the flow direction were neglected. Muthukumar *et al.* [25] explored insights of nanofluid with the Lorentz force in the cavity. They utilized the role of solar radiation to determine the variation in heat energy. Finite volume method has been implemented for numerical consequences. Shamshuddin *et al.* [26] studied nanofluid along with water-based fluid utilizing the role of MHD near a stretching plate. Shamshuddin *et al.* [27] discussed a numerical treatment related to micropolar fluid in the presence of nanofluid, thermal radiation, activation energy, and Hall forces on a stretching surface. Hayat *et al.* [28] determined the 3D mechanism of Williamson fluid toward a surface utilizing OHAM. Hayat *et al.* [29] deducted the influence of thermal role of Jeffrey fluid conspiring MHD and nanoparticles. They utilized active and passive approaches on surface. They used thermophoresis and Brownian motion. Figure 1a shows that nanofluid is used in a variety of industries. Nanofluid is utilized in wastewater treatment procedures, batteries for energy storage, and solar panels for energy generation. Additionally, it is used in paints and inks, drug delivery systems, cosmetics, and as a component of sunscreen. This adaptability emphasizes its significance in industries ranging from personal care and pharmaceuticals to renewable energy.

Table 1 compares the novelty work with published works [30–32]. From Table 1, it can be seen that tangent-hyperbolic Casson fluid, dusty fluid, and slip conditions adding tri-hybrid nanofluid have not been investigated yet in published works [30–32]. Moreover, Rana *et al.* [33] studied Newton fluid on the 3D surface using Finite element method (FEM) but tangent-hyperbolic Casson fluid and dusty fluid were not observed utilizing tri-hybrid nanofluid.

2 Analysis and modeling procedure

The 3D motion of tangent-hyperbolic Casson fluid is considered on the 3D-stretching wedge. A Darcy–Forchhiermer model is utilized to determine motion and heat energy.

Table 1: An investigation of novelty work

Authors	Tangent-hyperbolic Casson fluid	3D Wedge surface	Dusty fluid	Slip conditions	FEM	Tri-hybrid nanofluid
Rana and Gupta [30]	✗	✓	✗	✗	✓	✗
Kudenatti and Jyothi [31]	✗	✓	✗	✗	✗	✗
Kudenatti *et al.* [32]	✗	✓	✗	✗	✗	✗
Rana *et al.* [33]	✗	✓	✗	✓	✓	✗

The two-phase model is considered based on dusty fluid and phase liquid. The heat energy mechanism occurs using the aspects of heat sink and thermal radiation (variable). Slip conditions are employed for the current model. The correlations of tri-hybrid nanofluid are implemented with the suspension of silicon dioxide, copper, and Al_2O_3 with a base liquid called ethylene glycol. The geometry of the current problem is observed in Figure 1b. Thermal properties of nanofluid are displayed in Table 2.

- While non-Newtonian behavior (such as shear-thinning) can be represented by the tangent-hyperbolic model, real fluids might not always display such idealized features. Such an exact rheological model may not be followed by real fluids, particularly in situations with variable flow conditions;
- Although the Darcy–Forchheimer model works well for fluid flow in porous media, in real-world settings, the porous medium's structure can have a substantial impact on fluid behavior in ways that are challenging to describe using generalized equations;
- Although two-phase models are useful for modeling the behavior of suspended particles in a fluid, they are not well suited to represent the non-spherical shapes and agglomeration of real dust particles. Such as particle-fluid interactions can vary greatly in real-world applications, and dust particles may not behave as ideal passive tracers;
- Although the suspension of three distinct nanoparticles in ethylene glycol results in improved thermal properties, real-world applications need to take stability over time, sedimentation, and particle agglomeration into account.

A system associated with nonlinear ordinary differential equations (ODEs) [33,34] are

$$V_y + W_z + U_x = 0, \tag{1}$$

$$\begin{aligned} U_xU + U_yV + U_zW = {} & U_xU + V_xV + \nu_{\text{thnf}}[(1-n)(1+\beta^{-1})U_{zz} \\ & + 1 + \beta^{-1}\sqrt{2}n\Gamma^{\text{e}}U_zU_{zz}] \\ & + \frac{k^*N}{\rho_{\text{thnf}}}(V_y - V) - \frac{\sigma_{\text{thnf}(B_0)^2}}{\rho_{\text{thnf}}}(U) \\ & - \frac{\nu_{\text{thnf}}}{K^{\text{s}}}F_{\text{s}}U - \frac{F_{\text{s}}}{(K^{\text{s}})^{\frac{1}{2}}}F_{\text{s}}U, \end{aligned} \tag{2}$$

$$\begin{aligned} V_xU + V_yV + V_zW = {} & V_xU + V_yV + \nu_{\text{thnf}}[(1-n)(1+\beta^{-1})V_{zz} \\ & + (1+\beta^{-1})\sqrt{2}n\Gamma^{\text{e}}V_zV_{zz}] \\ & + \frac{k^*N}{\rho_{\text{thnf}}}(U_{\text{p}} - U) - \frac{\sigma_{\text{thnf}(B_0)^2}}{\rho_{\text{thnf}}}(V) \\ & - \frac{\nu_{\text{thnf}}}{K^{\text{s}}}F_{\text{s}}V - \frac{F_{\text{s}}}{(K^{\text{s}})^{\frac{1}{2}}}F_{\text{s}}V, \end{aligned} \tag{3}$$

$$\begin{aligned} T_xU + T_yV + T_zW = {} & \frac{K_{\text{thnf}}}{(\rho c_{\text{p}})_{\text{thnf}}}T_{zz} + \frac{\sigma_{\text{thnf}(B_0)^2}}{\rho_{\text{thnf}}}(U^2 + V^2) \\ & + \frac{\sigma^*16}{3(\rho c_{\text{p}})_{\text{thnf}}}[T^3T_{zz} + 3T^2(T_z)^2] \\ & + \frac{Q}{(\rho c_{\text{p}})_{\text{thnf}}}(T - T_\infty) + \frac{NC_{\text{pf}}\text{m}}{\rho c_{\text{p}}\tau_t}(T_{\text{p}} - T). \end{aligned} \tag{4}$$

Slip conditions for phase fluid [33] are

$$\begin{aligned} U &= U_w + l_1U_z, \quad V = V_w + l_2V_z, \quad W = 0, \\ & T = T_w + l_2\frac{\partial T}{\partial z} : z = 0, \\ & U \to u_\infty, \quad V \to v_\infty, \quad T \to T_\infty : z \to \infty. \end{aligned} \tag{5}$$

Boundary conditions (BCs) for the dusty flow model [35] are

$$u_{\text{p}} \to 0, v_{\text{p}} \to 0, \quad w_{\text{p}} \to W, \quad T_{\text{p}} \to T_\infty. \tag{6}$$

At $z = 0$, the BCs are as follows: velocity along the x-direction is $U_w + l_1U_z$, where U_w is the wall. At $z = 0$, the BCs state that the velocity (x-direction) is $U_w + l_1U_z$, where U_w is the wall velocity as it is generated under the slip condition. Velocity gradient, or l_1U_z, is generated under no-slip conditions. The changing linear velocity is shown by l_1. $V_w + l_2V_z$ is the velocity (x-direction). The wall velocity along the y-component is denoted by V_w. w indicates the velocity direction along the z-direction. l_2V_z describes the linear velocity gradient that describes potential slip or no-slip based on l_2. When $w = 0$, flow is not present. When $T = T_w$, the fluid's temperature at the wall and the wall's temperature are equal. The boundaries at $z \to \infty$, $U \to u_\infty$, and $V \to v_\infty$. The motivations of the problem are described as the proper setup of the problem about the interactions at the boundaries depending on these BCs. Proper modeling of multiphase flows, micro-scale heat transfer, and flows involving suspended particles or nanofluids depends on their ability to capture phenomena such as slip effects, rarefied gas behavior, dusty fluid dynamics, and thermal slip. Similarity variables [33] are

Table 2: Multiple nanofluidic thermal properties [36]

Properties	Aluminum oxide	Copper	Titanium oxide	Ethylene glycol
k	40	401	8.9538	0.253
ρ	3,970	8,933	4,250	1113.5
C_{p}	765	385	686.2	2,430

$$
\begin{aligned}
U &= u_\infty (x+y)^n \frac{\partial F}{\partial \eta}, \quad V = v_\infty (x+y)^n \frac{\partial G}{\partial \eta}, \\
\eta &= \left(\frac{U(1+n)\nu_f}{(x+y)2\nu_f}\right)^{1/2} z, \quad T = \Theta(T_w - T_\infty) + T_\infty, \\
W &= -\left(\frac{u_f(1+n)\nu_f}{2}\right)^{\frac{1}{2}} (x+y)^{\frac{n-1}{2}} \left[F + \gamma G \right. \\
&\quad \left. + \frac{n-1}{n+1}\eta\left(\frac{\partial F}{\partial \eta} + \gamma \frac{\partial G}{\partial \eta}\right)\right], \\
T_p &= (T_w - T_\infty)\Theta_p + T_\infty, \\
u_p &= u_\infty (x+y)^n f', \quad v_p = v_\infty (x+y)^n g', \\
w_p &= -\left(\frac{\mathbb{U}_\infty (1+n)\nu_f}{2}\right)^{\frac{1}{2}} (x+y)^{\frac{n-1}{2}} (f+g).
\end{aligned} \tag{7}
$$

By converting the governing partial differential equations (PDEs) into ODEs, similarity transformations are specially made to minimize the number of independent variables. When a transformation satisfies the continuity equation, this simplification is possible. The similarity transformations are based on several assumptions such as boundary layer approximations, constant properties, and scaling symmetry. Further, assumptions affect the flow behavior. Such assumptions are investigated as the impact on nonlinear impact, the validity of boundary layer, and reduction in complexity. When such assumptions are implemented, nonlinear effects may be approximated, which can influence the overall accuracy of the solution. The solution is specific to certain configurations because the similarity variable is frequently derived based on the flow geometry. Using similarity variables, the formulation of ODEs is

$$
\begin{aligned}
&(1+\beta^{-1})\left[(1-m)\frac{\partial^3 F}{\partial \eta^3} + m\mathrm{We}\frac{\partial^2 F}{\partial \eta^2}\frac{\partial^3 F}{\partial \eta^3}\right] \\
&- \frac{\partial^2 F}{\partial \eta^2}(F+\gamma G) + B^*\left(1 - \left(\frac{\partial F}{\partial \eta}\right)^2\right) \\
&+ \gamma B^*\left(1 - \frac{\partial F}{\partial \eta}\frac{\partial G}{\partial \eta}\right) + \delta_1 \gamma_1 (f' + F) \\
&- M^2 \frac{\partial F}{\partial \eta} - \epsilon \frac{\partial F}{\partial \eta} - \mathrm{Fr}\left(\frac{\partial F}{\partial \eta}\right)^2 = 0,
\end{aligned} \tag{8}
$$

$$
\begin{aligned}
&(1+\beta^{-1})\left[(1-m)\frac{\partial^3 G}{\partial \eta^3} + m\mathrm{We}\frac{\partial^2 G}{\partial \eta^2}\frac{\partial^3 G}{\partial \eta^3}\right] \\
&- \frac{\partial^2 G}{\partial \eta^2}(F+\gamma G) + B^*(1 - GF) \\
&+ \gamma B^*\left(1 - \left(\frac{\partial G}{\partial \eta}\right)^2\right) + \delta_1 \gamma_1 \left(g' + \frac{\partial G}{\partial \eta}\right) \\
&- M^2 \frac{\partial G}{\partial \eta} - \in \frac{\partial G}{\partial \eta} - \mathrm{Fr}\left(\frac{\partial G}{\partial \eta}\right)^2 = 0,
\end{aligned} \tag{9}
$$

$$
\begin{aligned}
&\frac{\partial^2 \Theta}{\partial \eta^2} + \mathrm{Pr}\,\mathrm{Nr}\left[\{(T_r - 1)\Theta + 1\}^3 \frac{\partial^2 \Theta}{\partial \eta^2}\right. \\
&\left. + 3(T_r - 1)\{(T_r - 1)\Theta + 1\}^2 \left(\frac{\partial \Theta}{\partial \eta}\right)^2\right] \\
&+ \frac{\partial \Theta}{\partial \eta}(F + \gamma G) + \frac{k_f}{k_{thnf}} M^2 \mathrm{EcPr}\left(\left(\frac{\partial F}{\partial \eta}\right)^2 + \left(\frac{\partial G}{\partial \eta}\right)^2\right) \\
&- \lambda \delta_t \mathrm{Pr}(\Theta'_p - \Theta) = 0.
\end{aligned} \tag{10}
$$

The correlations of tri-hybrid nanofluid [36] are derived as

$$
\frac{\mu_f}{(1-\phi_{Al_2O_3})^{2.5}(1-\phi_{Cu})^{2.5}(1-\phi_{TiO_2})^{2.5}} = \mu_{thnf}, \tag{11}
$$

$$
\begin{aligned}
\rho_{thnf} &= (1-\phi_{Al_2O_3})\{(1-\phi_{Cu})[(1-\phi_{TiO_2})\rho_f + \phi_{TiO_2}\rho_{TiO_2}] \\
&\quad + \phi_{Cu}\rho_{Cu}\} + \phi_{Al_2O_3}\rho_{Al_2O_3},
\end{aligned} \tag{12}
$$

$$
\begin{aligned}
\frac{K_{hb}}{K_{nf}} &= \frac{K_{Cu} + 2K_{nf} - 2\phi_{Cu}(K_{nf} - K_{Cu})}{K_{Cu} + 2K_{nf} + \phi_{Cu}(K_{nf} - K_{Cu})}, \\
\frac{K_{thb}}{K_{hb}} &= \frac{K_{Al_2O_3} + 2K_{hb} - 2\phi_{Al_2O_3}(K_{hb} - K_{Al_2O_3})}{K_{Al_2O_3} + 2K_{hb} + \phi_{Al_2O_3}(K_{hb} - K_{Al_2O_3})},
\end{aligned} \tag{13}
$$

$$
\begin{aligned}
\frac{K_{nf}}{K_f} &= \frac{K_{TiO_2} + 2K_f - 2\phi_{TiO_2}(K_f - K_{TiO_2})}{K_{TiO_2} + 2K_f + \phi_{TiO_2}(K_f - K_{TiO_2})}, \\
\frac{\sigma_{nf}}{\sigma_f} &= \frac{\sigma_{TiO_2}(1 + 2\phi_{TiO_2}) + \phi_f(1 - 2\phi_{TiO_2})}{\sigma_{TiO_2}(1 - \phi_{TiO_2}) + \sigma_f(1 + \phi_{TiO_2})},
\end{aligned} \tag{14}
$$

$$
\begin{aligned}
\frac{\sigma_{thnf}}{\sigma_{hb}} &= \frac{\sigma_{Al_2O_3}(1 + 2\phi_{Al_2O_3}) - \mathscr{F}_{hb}(1 - 2\phi_{Al_2O_3})}{\sigma_{Al_2O_3}(1 - \phi_{Al_2O_3}) + \sigma_{hb}(1 + \phi_{Al_2O_3})}, \\
\frac{\sigma_{hb}}{\sigma_{nf}} &= \frac{\sigma_{Cu}(1 + 2\phi_{Cu}) + \varphi_{nf}(1 - 2\phi_{Cu})}{\sigma_{Cu}(1 - \phi_{Cu}) + \sigma_{nf}(1 + \phi_{Cu})}.
\end{aligned} \tag{15}
$$

Developing a model associated with the dusty fluidic model [35] is

$$
(v_p)_y + (w_p)_z + (u_p)_x = 0, \tag{16}
$$

$$
u_p(u_p)_x + v_p(u_p)_y + w_p(u_p)_z = \frac{Kn}{\rho_p}(u - u_p), \tag{17}
$$

$$
u_p(v_p)_x + v_p(v_p)_y + w_p(v_p)_z = \frac{Kn}{\rho_p}(v - v_p), \tag{18}
$$

$$
(T_p)_x u_p + (T_p)_y v_p + (T_p)_z w_p = \frac{c_p}{c_m \tau_t}(T - T_p). \tag{19}
$$

Formulation of the dusty fluidic model is

$$
(f+g)\frac{\partial^2 f}{\partial \eta^2} - \left(\frac{\partial f}{\partial \eta}\right)^2 - \frac{\partial g}{\partial \eta}\frac{\partial f}{\partial \eta} + \delta_v\left(\frac{\partial F}{\partial \eta} - \frac{\partial f}{\partial \eta}\right) = 0, \tag{20}
$$

$$
(f+g)\frac{\partial^2 g}{\partial \eta^2} - \left(\frac{\partial g}{\partial \eta}\right)^2 - \frac{\partial g}{\partial \eta}\frac{\partial f}{\partial \eta} + \delta_v\left(G - \frac{\partial g}{\partial \eta}\right) = 0, \tag{21}
$$

$$(f+g)\frac{\partial \Theta_p}{\partial \eta} + \lambda\delta_t(\Theta - \Theta_{\mathrm{p}}) = 0. \tag{22}$$

BCs for phase fluid [33,35] are

$$\begin{aligned} &F = 0, \quad G = 0, \quad \frac{\partial F}{\partial \eta} = \lambda_1 + \alpha_1\frac{\partial^2 F}{\partial \eta^2}, \\ &\frac{\partial G}{\partial \eta} = \lambda_2 + \alpha_2\frac{\partial^2 G}{\partial \eta^2}, \Theta = 1 + \alpha_3\frac{\partial \Theta}{\partial \eta} : \eta = 0, \\ &\frac{\partial \mathrm{F}}{\partial \eta} \to 1, \quad \frac{\partial \mathrm{G}}{\partial \eta} \to 1, \Theta \to 0 : \eta \to \infty. \end{aligned} \tag{23}$$

BCs of dusty fluid are

$$F = f, G' \to 0, \quad G = g, \quad F' \to 0, \Theta_p \to 0 : \eta \to \infty. \tag{24}$$

Divergent velocities on the surface [33] are

$$\mathrm{Cf}_x = \frac{\tau_{xz}}{(u_w)^2\rho_{\mathrm{thnf}}},$$

$$(\mathrm{Re})^{-\frac{1}{2}}\mathrm{Cf}_x = \nu_{\mathrm{thnf}}(1+\beta^{-1})\left[(1-n)\frac{\partial^2 F}{\partial \eta^2}(0) + \frac{n}{2}\mathrm{We}\frac{\partial^2 F}{\partial \eta^2}(0)\right], \tag{25}$$

$$\mathrm{Cf}_y = \frac{\tau_{yz}}{(u_w)^2\rho_{\mathrm{thnf}}},$$

$$(\mathrm{Re})^{-\frac{1}{2}}\mathrm{Cf}_y = \nu_{\mathrm{thnf}}(1+\beta^{-1})\left[(1-n)\frac{\partial^2 G}{\partial \eta^2}(0) + \frac{n}{2}\mathrm{We}\frac{\partial^2 G}{\partial \eta^2}(0)\right], \tag{26}$$

Nusselt number [33] is

$$(\mathrm{Re})^{-\frac{1}{2}}\mathrm{Nu} = -\left(\frac{K_{\mathrm{thnf}}}{k_{\mathrm{f}}} + \mathrm{Nr}\{1+(T_{\mathrm{r}}-1)\Theta(0)\}^3\right)\frac{\partial \Theta}{\partial \eta}(0). \tag{27}$$

3 Numerical procedure (FEM)

A strong numerical method for resolving challenging physical and engineering problems is the FEM. It allows for the accurate approximation of solutions by decomposing complex geometries into smaller, more manageable components. FEM is especially dependable for applications in fluid dynamics and structural analysis because of its well-known consistency, stability, and convergence. Because of its versatility, this approach allows simulations to be conducted in a range of geometries and conditions. FEM is now a vital tool in domains like material science, thermal analysis, and computational mechanics due to its accuracy and adaptability. Due to several benefits, FEM [36] is frequently used to solve ODEs, particularly in engineering and physics.

- Complex and irregular geometries are well suited for the Galerkin FEM's application. Because of its flexible meshing capabilities due to the use of finite elements, it is easier to model complex shapes that may be difficult to handle with finite difference or finite volume methods;
- FEM is very flexible when it comes to various BCs;
- When approximating functions for a problem can use higher-order polynomials, the Galerkin FEM typically produces results with high accuracy;
- Galerkin FEM works well for nonlinear problems, where it can approximate solutions through a variety of well-convergent iterative techniques.

A computational domain with smaller subdomains is depicted in Figure 1c and d. A line segment connecting points O and P in Figure 1c denotes a portion of the computational domain, and an arrow pointing from O to P may suggest flow. The domain is divided into segments below by a series of nodes ranging from H_1, H_2, $H_3 \ldots H_n$, with two nodes enclosing each segment. As Figure 1d suggests, this segmentation makes it possible to solve boundary value problems over a semi-infinite domain. By establishing a structure that allows computations to be done, the nodes and subdomains make numerical analysis easier.

It is investigated that P satisfies the BCs and OP is termed as the computation domain. Moreover, line segments divide into elements (Dom_i).

$$\mathrm{Dom}_i = [\eta_i, \eta_{i+1}, \eta_i]. \tag{28}$$

BVP is

$$KL = 0, \xi \in D. \tag{29}$$

The discretization procedure is

$$\int K\left(\sum_{i=1}^{n} H_i\Psi_i\right)\Psi_j \mathrm{d}\Omega = 0. \tag{30}$$

The system of the equations is derived as

$$AH_i = b. \tag{31}$$

A is termed as matrix which have order $n \times n$ along with nodal values (H_i). Weights are utilized and get residuals. A particular element's weighted residuals are integrated.

$$L_{\mathrm{h}} = \sum_{i=1}^{n} H_i\Psi_i, \tag{32}$$

where $H_i = F_i,\ K_i, \Theta_i$. Convergence criteria is given as

$$\mathrm{maX}|\pi_i^{rr} - \pi_i^{rr-1}| < 10^{-5}. \tag{33}$$

Table 4 reveals a comparative study of divergent velocities with published work [33] when $\phi_{Al_2O_3} = \phi_{Cu} = \phi_{TiO_2}$, We = 0, and $\beta \to \infty$. Table 3 shows the grid size analysis of the present problem.

Table 3: Grid sizes analysis of $\Theta_{\mathrm{p}}\left(\frac{\eta_{\max}}{2}\right)$, $\mathscr{g}_{\mathrm{p}}\left(\frac{\eta_{\max}}{2}\right)$, $\mathscr{F}_{\mathrm{p}}\left(\frac{\eta_{\max}}{2}\right)$, $\mathscr{g}'$, and $\mathscr{F}'\left(\frac{\eta_{\max}}{2}\right)$

e	$\frac{\partial F}{\partial \eta}\left(\frac{\eta_{\max}}{2}\right)$	$\frac{\partial G}{\partial \eta}\left(\frac{\eta_{\max}}{2}\right)$	$\frac{\partial \Theta}{\partial \eta}\left(\frac{\eta_{\max}}{2}\right)$	$f\left(\frac{\eta_{\max}}{2}\right)$	$g\left(\frac{\eta_{\max}}{2}\right)$	$\Theta_{\mathrm{p}}\left(\frac{\eta_{\max}}{2}\right)$
30	0.0263056813	0.468037679	0.9787987450	0.2827906191	0.9728469816	0.4434560857
60	0.1024126448	0.613468134	0.9011902284	0.2757838387	0.9241008486	0.3894606208
90	0.4608096422	0.729510739	0.8575691334	0.2689178444	0.8616644350	0.3795863152
120	0.9087343128	0.841304991	0.6280278959	0.2396007177	0.6852125089	0.3699807236
150	0.5366047203	0.869142734	0.4382757165	0.2154342127	0.6627948456	0.3606296076
180	0.6732862104	0.962055210	0.3579070710	0.1819296553	0.6417161658	0.2860406550
210	0.7074475637	0.985035534	0.3491410437	0.1511252426	0.6218255025	0.2714070159
240	0.7603237962	0.987016648	0.3496053880	0.1248266455	0.5363569043	0.2105439010
270	0.7615670843	0.987858170	0.3496873858	0.1242190043	0.5362886906	0.2121636134
300	0.7611427340	0.987822332	0.3496175284	0.1246608994	0.5363221069	0.2124366880

Table 4: Comparative study of divergent velocities with published work [33] when $\mathscr{o}_{Al_2O_3} = \mathscr{o}_{Cu} = \mathscr{o}_{TiO_2}$, We = 0, and $\beta \to \infty$

	Rana *et al.* [33]	FEM
$\mathscr{F}''(0)$	0.64479203	0.6444041881
$\mathscr{g}''(0)$	0.76390721	0.7639055017

4 Results and discussion

The features of hyperbolic tangent Casson liquid are visualized using a phase model based on the fluidic phase and dusty phase on the 3D wedge. Several aspects related to thermal radiation (variable), multiple conditions, and heat sink are considered. The comparison between the fluidic phase and dusty phase is observed with various parameters on fluidic motion and thermal energy. The numerical values of

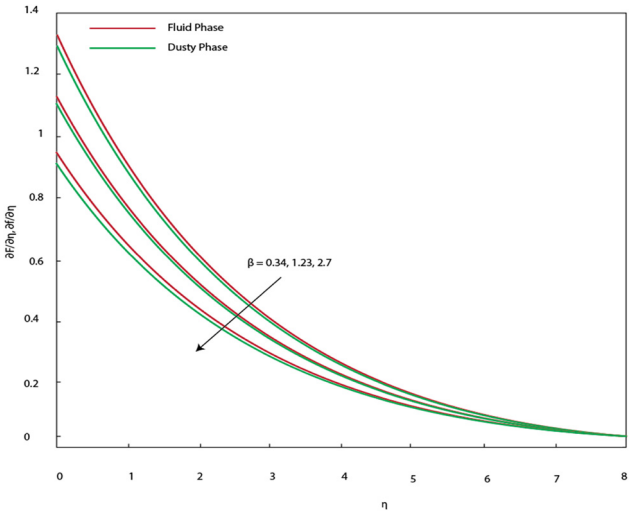

Figure 3: Velocity curves (along *x*-axis) under variation in β.

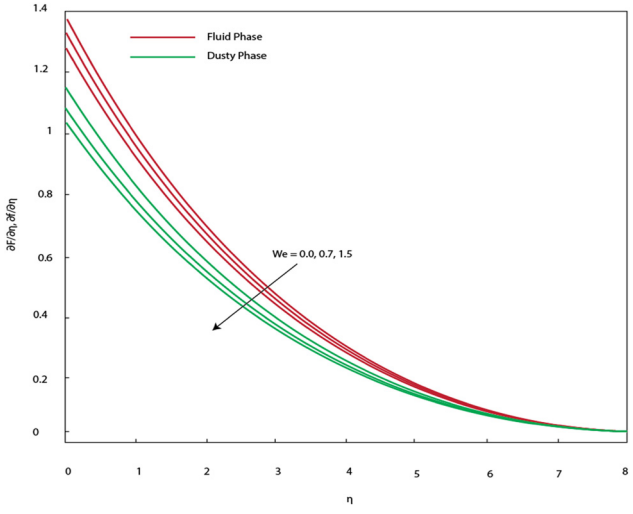

Figure 2: Velocity curves (along *x*-axis) under variation in We.

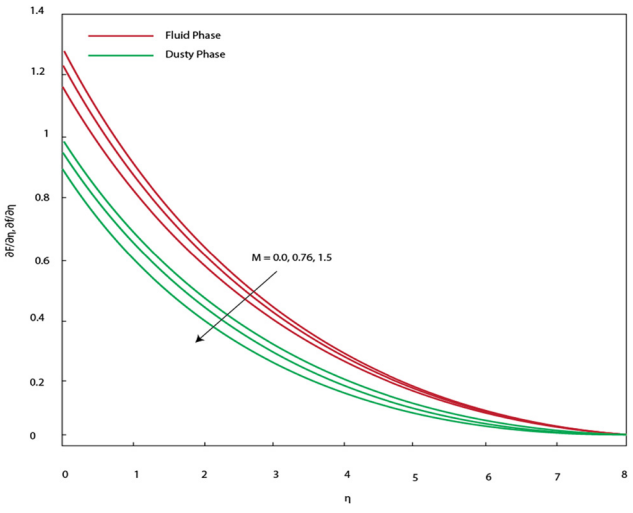

Figure 4: Velocity fields (along *x*-axis) under variation in M.

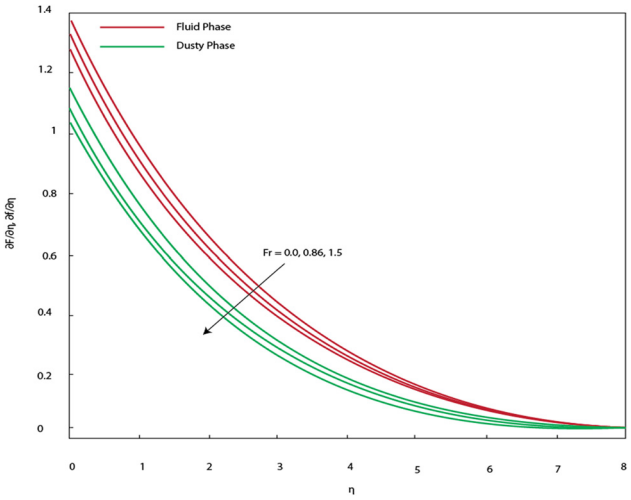

Figure 5: Velocity fields (along *x*-axis) under variation in Fr.

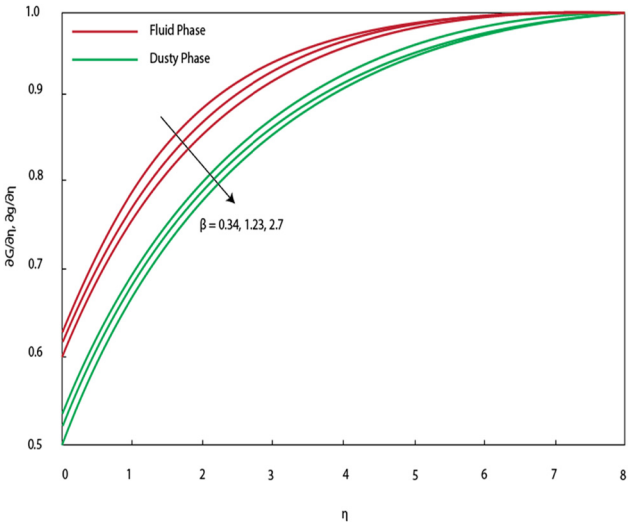

Figure 7: Velocity fields (along *y*-axis) under variation in β.

parameters are adopted based on published works [32,33], publishing works suggest the selecting parameters. Further, FEM is utilized for analyzing the numerical results. The selection of parameter ranges can be influenced by the fact that mesh independence studies are frequently carried out by adjusting the mesh parameters until the results converge. The ranges of parameters are $0.3 \le \beta \ge \infty$, $0.0 \le m \ge 10$, $0.0 \le \mathrm{We} \ge 15$, $0 \le \beta^* \ge 1$, $0 \le \delta_1 \ge 1.5$, $0 \le \delta_1 \ge 2.5$, $0.0 \le \mathrm{Fr} \ge 5.0$, $0.0 \le \epsilon \ge 3.0$, $0.0 \le \mathrm{Nr} \ge 10$, $1.5 \le \mathrm{Pr} \ge 10$, $0.0 \le T_r \ge 5$, $0.0 \le \mathrm{Ec} \ge 7.0$, $0.0 \le \phi_{\mathrm{Cu}} \le 0.07$, $0.0 \le \phi_{\mathrm{TiO_2}} \le 0.05$, $0 \le \phi_{\mathrm{Al_2O_3}} \le 0.06$, $0.0 \le \lambda_2 \le 1.5$, $0.0 \le \lambda_1 \le 2.0$, $0 \le \alpha_1 \le 3.0$, $0 \le \alpha_2 \le 2.4$, $0 \le \alpha_3 \le 3.5$. The numerical outcomes are estimated using FEM. Detailed discussion and explanations are given below.

The impacts of We, β, M, and Fr on velocity fields associated with the dusty phase and fluidic phase models are observed in Figures 2–9. The fluidic phase model is illustrated by red lines while green lines show the impact of the dusty phase. The illustration of We on velocity fields (primary and secondary) associated with the dusty phase and fluidic phase model is observed in Figures 2 and 6 (primary and secondary). The velocity fields decreased when We is enhanced for the dusty phase and fluidic phase model. The flow behavior of non-Newtonian fluids, especially those with viscoelastic properties, is described by this dimensionless number (We). It shows that elastic and viscous forces are present in a flowing material. Moreover, the dusty phase on the velocity of the fluid is less than the fluid phase on the velocity field. Figures 3 and 7 (primary and secondary) reveal the impact of β on velocity

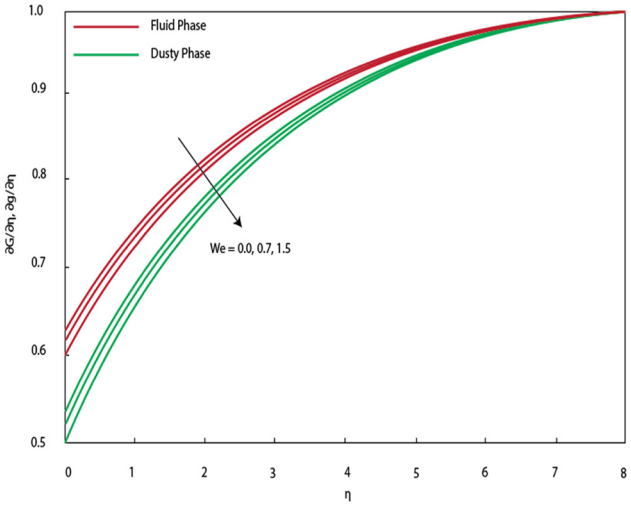

Figure 6: Velocity fields (along *y*-axis) under variation in We.

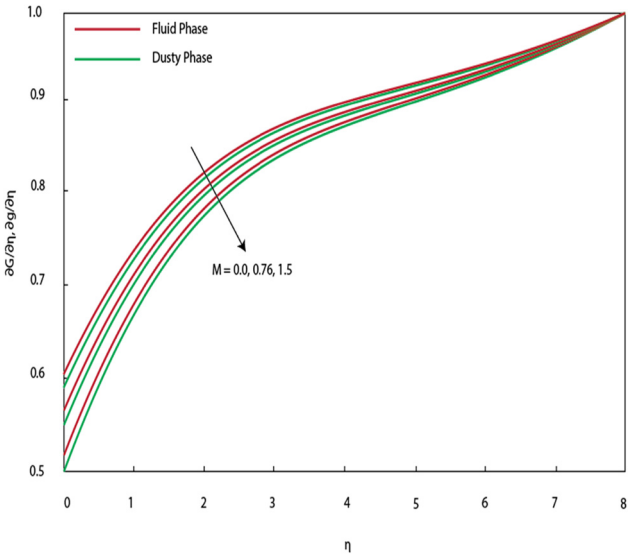

Figure 8: Velocity fields (along *y*-axis) under variation in M.

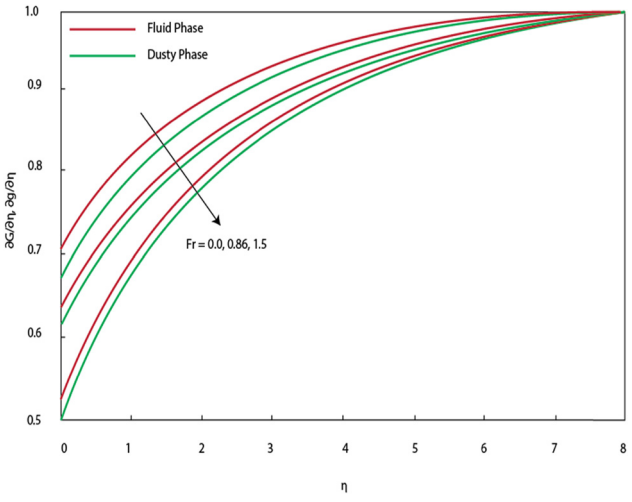

Figure 9: Velocity fields (along *y*-axis) under variation in Fr.

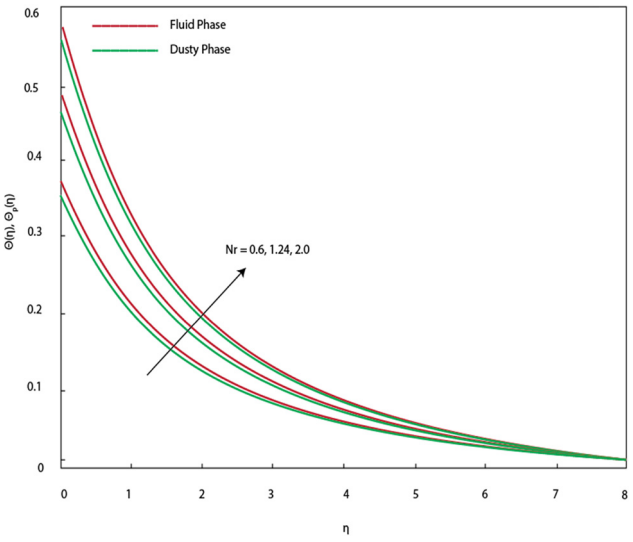

Figure 11: Velocity curves under variation in Nr.

fields (primary and secondary) associated with the dusty phase and fluidic phase. By increasing the values of β, a decrease in the velocity field occurs. The occurrence of β is modeled using the modeling of the Casson fluid. The occurrence of β appears due to non-Newtonian fluid in the momentum equations. $\beta = 0$ is called Newtonian fluid while $\beta > 0$ is called non-Newtonian fluid. The flow for $\beta = 0$ is greater than the flow for $\beta > 0$. Figures 4 and 8 (primary and secondary) describe the influence of magnetic number on velocity fields associated with the fluidic phase and dusty phase. The generation of M is formulated utilizing the idea of the Lorentz force. The Lorentz force is the force experienced by a charged particle moving through an electric and magnetic field. The fluid's velocity field can be significantly affected by the magnetic parameter when it flows in the presence of a magnetic field. The Lorentz force resists the motion of an electrically conducting fluid when a magnetic field is applied to it, especially when the fluid is moving perpendicular to the direction of the magnetic field. Dusty phase fluidic motion is less than fluidic motion. Figures 5 and 9 (primary and secondary) illustrate the influence of Fr on velocity fields associated with dusty phase and fluidic phase models. The dimensionless parameter known as the Darcy–Forchheimer number and fluid mechanics express that both Forchheimer and Darcy's laws affect a fluid's flow through a porous medium. It takes into consideration the combined effects of inertial and viscous forces on the flow within the medium. Figure 10 describes the impact of magnetic number on velocity fields associated with dusty and

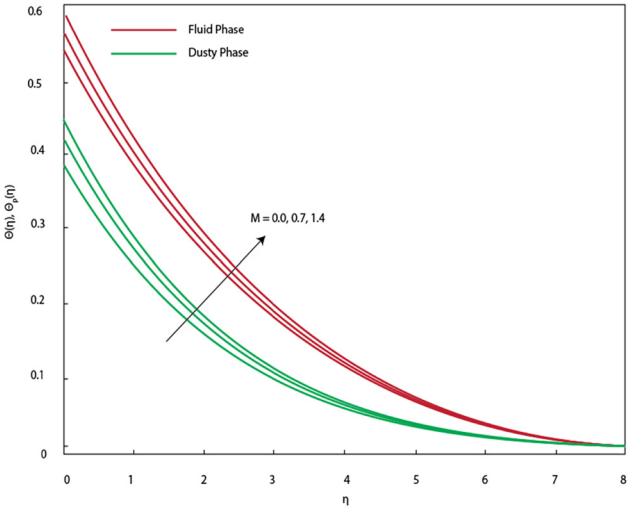

Figure 10: Temperature curve under variation in M.

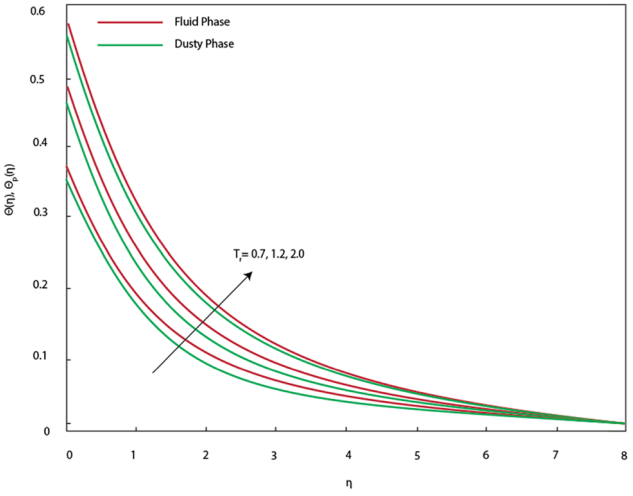

Figure 12: Temperature curve under variation in T_r.

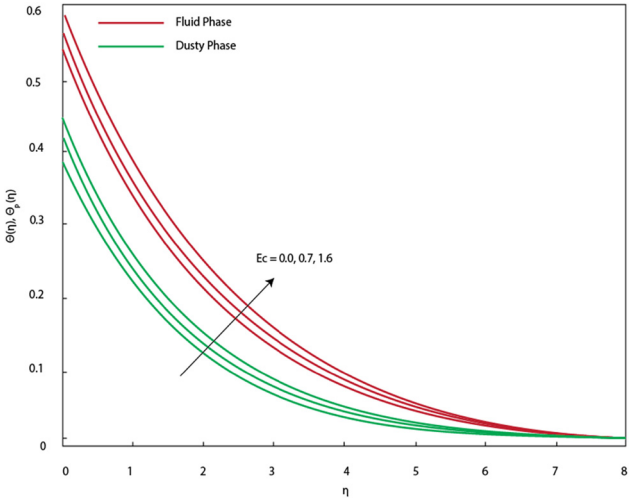

Figure 13: Temperature curve under variation in Ec.

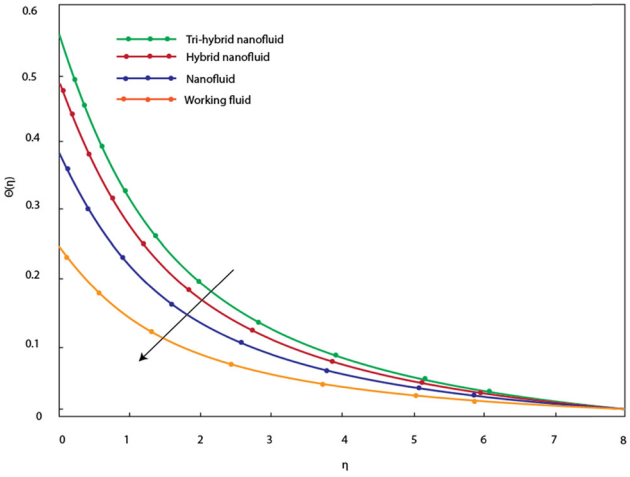

Figure 14: The comparative roles of nanofluid, tri-hybrid, hybrid nanofluid, and working material.

fluidic phases. The moving electrons collide with ions in a conductor when an electric current passes through a conductor with electrical resistance. These collisions create resistance to the flow of electrons, which leads to the production of heat. The conductor's resistance and the current's magnitude determine how much heat is produced. The heat energy is dissipated when the magnetic number is increased. The temperature curve for the dusty phase is less than the temperature curve for the fluidic phase. Figure 11 captures the aspects of thermal radiation number (Nr) on the temperature region associated with dusty and fluidic layers. The thermal radiation number represented as Nr is a dimensionless parameter that measures the proportion of thermal radiation to conduction. It facilitates comprehension of the impact of radiative heat transfer in situations where thermal radiation interacts with other mechanisms of heat transfer. The dominance of radiative heat transfer over conductive heat transfer is indicated by a high thermal radiation number. This is frequently observed in systems operating at high temperatures where thermal radiation is important. When analyzing and modeling heat transfer problems, the thermal radiation number comes in handy, particularly in high-temperature applications or when surfaces with significant temperature differences are involved. An influence of T_r on temperature region associated with dusty and fluidic phase is observed. An inclination of thermal energy is produced

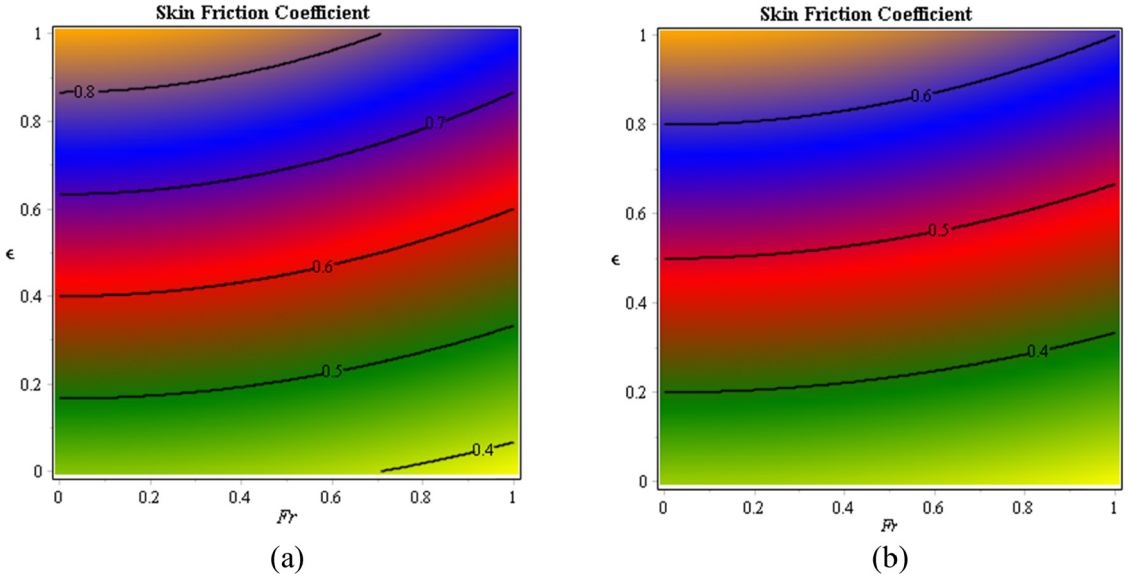

Figure 15: Impacts of ϵ and Fr on divergent velocities for (a) fluid phase and (b) dusty phase.

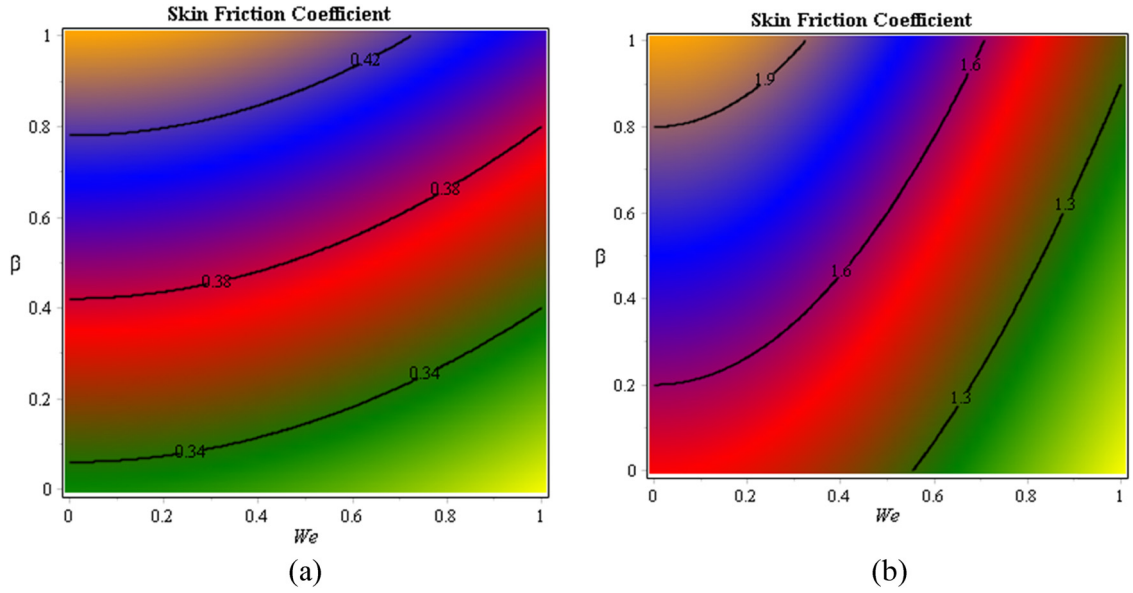

Figure 16: Impacts of We and β on divergent velocities for (a) fluid phase and (b) dusty phase.

when T_r is increased. The ratio of the surface temperature to the surrounding fluid temperature is represented by this parameter. Because it influences how thermal radiation affects the temperature distribution, it is important to the thermal field. Nonlinear thermal radiation suggests that the radiation-induced heat transfer follows a more complicated relationship, frequently involving higher powers of temperature, rather than being directly proportional to the temperature difference. An influence of T_r on temperature region associated with dusty and fluidic phase is shown in Figure 12. An increase of thermal energy is produced when T_r is increased. The ratio of the surface temperature to the surrounding fluid temperature is represented by this parameter. Because it influences how thermal radiation affects the temperature distribution, it is important to the thermal field. Nonlinear thermal radiation suggests that the radiation-induced heat transfer follows a more complicated relationship, frequently involving higher powers of temperature, rather than being directly proportional to the temperature difference. The behavior of Eckert number on the

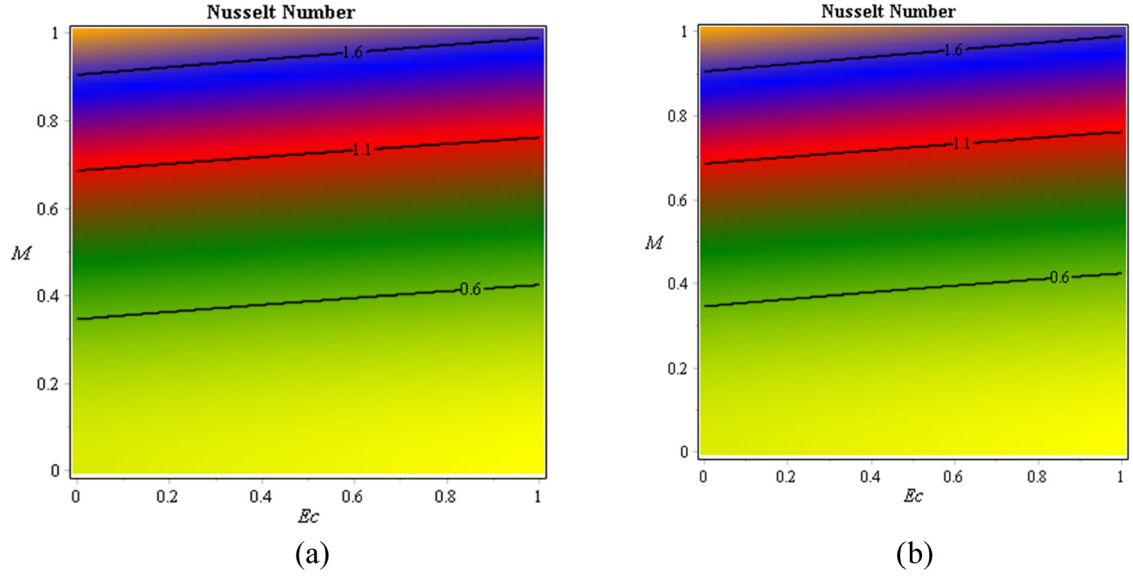

Figure 17: Impacts of Ec and M on Nusselt number for (a) fluid phase and (b) dusty phase.

Table 5: Change in Ec, γ_*, T_r, Nr, and M on temperature gradient for the cases of dusty fluid and phase liquid

		Dusty fluid $(\mathbf{Re})^{-\frac{1}{2}}\mathbf{Nu}$	Phase fluid $(\mathbf{Re})^{-\frac{1}{2}}\mathbf{Nu}$
	0.0	0.36480028102	1.770151802
Ec	0.34	0.23884933983	1.731218232
	1.23	0.19109880902	1.713546962
	0.0	0.57479635041	1.834435685
γ_*	0.4	0.5258518684	1.824797872
	1.34	0.51163619783	1.814642557
	1.0	0.41612366681	1.757776531
T_r	2.0	0.30144899232	1.723305665
	3.0	0.24239392512	1.799752638
	0.0	0.34935000212	2.215742836
Nr	0.54	0.31407343313	2.131282652
	1.23	0.30979114713	2.046378252
	0.0	0.68881671303	2.061035594
M	0.45	0.51278152041	2.035260438
	1.23	0.34762525834	2.019058348

temperature curve associated with dusty as well as fluidic phases is addressed in Figure 13. The modeling of Eckert number is formulated using the idea of viscous dissipation. Viscous forces within the fluid cause the kinetic energy of fluid motion to be converted into thermal energy, a process known as viscous dissipation. Friction between fluid particles as they pass one another causes heat to be produced, raising the fluid's temperature overall during this process. Maximum heat energy can be generated when Ec is increased. The comparative roles of tri, di hybrid nanofluid, nanofluid, and working fluid are shown in Figure 14. Tri-hybrid nanofluids comprise three distinct kinds of nanoparticles, such as metal or metal oxide particles Cu, Al_2O_3, and graphene oxide, which are frequently chosen for their high thermal conductivities. This mixture improves thermal conductivity considerably more than single or bi-hybrid nanofluids when dissolved in a base fluid. To meet the demands of high-performance cooling applications, the resulting thermal performance is highly efficient when combined with a non-Newtonian base fluid, which frequently has inherent shear-thinning or shear-thickening properties. It is noticed that hybrid and tri-hybrid nanofluids have significantly improved the base fluid's heat transfer capabilities. The potential of tri-hybrid nanofluids is to have high-efficiency thermal management systems rather than hybrid nanofluids. The impacts of $\in$ and Fr on divergent velocities for the fluid phase and dusty phase are addressed in Figure 15a and b. The divergent velocities are increased when $\in$ and Fr are enhanced. Increased Forchheimer number signifies a dominance of inertial effects over viscous forces. This change results in a decrease in the skin friction coefficient because the flow is less impacted by the frictional resistance of the surface. Impacts of We and β on divergent velocities for the fluid phase and dusty phase are estimated in Figure 16a and b. The fluid responds more strongly to the shear forces at the boundary when β increases, leading to a higher skin friction coefficient at the wall due to increased shear stress. There is an increase in divergent velocities when We and β are increases. Influences of Ec and M on Nusselt number for the fluid phase and dusty phase are

Table 6: Change in M, We, β, Fr, and $\in$ on velocity gradients for the cases of TiO_2/Al_2O_3/Cu-EG and Al_2O_3/Cu-EG

		Al_2O_3/Cu-EG		TiO_2/Al_2O_3/Cu-EG	
		$-(\mathbf{Re})^{-\frac{1}{2}}\mathbf{Cf}_x$	$-(\mathbf{Re})^{-\frac{1}{2}}\mathbf{Cf}_y$	$-(\mathbf{Re})^{-\frac{1}{2}}\mathbf{Cf}_x$	$-(\mathbf{Re})^{-\frac{1}{2}}\mathbf{Cf}_y$
	0.0	0.7174098524	0.2380845076	1.1201236762	1.5288464948
M	0.34	0.7453276371	0.2444387401	1.1331270167	1.7422870413
	1.23	0.7572638292	0.2577989718	1.1785213659	1.8383011550
	0.0	0.5722686636	0.2512745187	1.1039612462	1.0207289972
We	0.15	0.5049598026	0.2448606745	1.0994454289	1.0750089459
	1.04	0.4114861279	0.2143042602	1.0827522130	1.0238428649
	0.0	0.3965478100	0.2084693574	1.03834210622	1.4553221069
β	0.24	0.3869438858	0.2327187697	1.04397237237	1.4748101256
	1.5	0.3976041228	0.2970495034	1.07749123875	1.4972352574
	0.0	0.3685131256	0.1698281517	1.07321802881	1.7348312940
Fr	0.3	0.3817118095	0.1745917073	1.08898175959	1.8316307591
	1.67	0.3984600091	0.1894193573	1.09269465380	1.9029960621
	0.0	0.2895538095	0.1543090817	1.05854685701	1.4851203247
$\in$	0.874	0.2922557514	0.1696242909	1.07443297878	1.4981063249
	2.0	0.3851014714	0.1748488622	1.08035222418	1.5518747894

addressed in Figure 17a and b. When Ec and M are enhanced, the Nusselt number decreases. Decrease in Nusselt number occurs when Ec and M are increased. The changes in Ec, γ_*, T_r, Nr, and M on temperature gradient for the cases of dusty fluid and phase liquid are recorded in Table 4. From Table 5 shows the temperature gradient decreases when M, Nr, T_r, and Ec are increased. Moreover, the temperature gradient for dusty fluid is less than the temperature gradient for phase fluid. Table 6 shows the change in M, We, β, Fr, and $\in$ on temperature gradient for the cases of TiO_2/Al_2O_3/Cu-EG and Al_2O_3/Cu-EG. From this table, it is noticed that skin friction coefficients decrease when M, We, β, Fr, and $\in$ are enhanced.

5 Conclusion

Features of ternary hybrid nanoparticles in dusty fluid on the 3D wedge and hyperbolic tangent Casson rheology are investigated. The Darcy's and Forchhiermer's laws are utilized. When visualizing thermal energy, nonlinear thermal radiations are taken into consideration. A heat sink and Joule heating are assumed with multiple slip constraints. For numerical purposes, FEM is used. Below is a list of the main conclusions.

- By increasing the values of We, β, M, and Fr, the velocity field and Momentum boundary layer thickness are suppressed;
- The fluidic phase on fluidic motion is higher than the dusty phase;
- The Lorentz force and thermal radiation bring declination of thermal energy and thermal boundary thickness;
- The fluid phase on the Nusselt number and the skin friction coefficient are higher than the dusty phase on the Nusselt number and skin friction coefficient;
- The heat transfer rate for ternary hybrid nanofluid is larger than that for hybrid nanofluid;
- Thermal energy for the fluid phase is greater than thermal energy for dusty phase. Hence, a fluid phase has significant energy rather than dusty fluid.

Acknowledgments: The authors extend their appreciation to Taif University, Saudi Arabia, for supporting this work through project number (TU-DSPP-2024-33).

Funding information: This research was funded by Taif University, Saudi Arabia, Project No. (TU-DSPP-2024-33).

Author contributions: U.N.: conceptualization, methodology, software, formal analysis, validation; and writing – original draft. U.K.: conceptualization, writing – original draft, writing – review and editing, supervision, and resources. H.A.: validation, investigation, writing – review and editing, formal analysis; project administration, and funding acquisition. H.G.: validation, writing – review and editing, software, conceptualization, and provided significant feedback and assisted in the revised version of the manuscript. All authors have accepted responsibility for the entire content of this manuscript and approved its submission.

Conflict of interest: The authors state no conflict of interest.

Data availability statement: The datasets used and/or analyzed during the current study are available from the corresponding author upon reasonable request.

References

[1] Bilal S, Sohail M, Naz R. Heat transport in the convective Casson fluid flow with homogeneous–heterogeneous reactions in Darcy–Forchheimer medium. Multidiscip Model Mater Struct. 2019;15(6):1170–89.

[2] Sohail M, Alrabaiah H, Ali U, Zohra FT, Selim MM, Thounthong P. Numerical exploration of thermal and mass transportation by utilising non-Fourier double diffusion theories for Casson model under Hall and ion slip effects. Pramana. 2021;95:1–12.

[3] Malik MY, Salahuddin T, Hussain A, Bilal S. MHD flow of tangent hyperbolic fluid over a stretching cylinder: Using Keller box method. J Magn Magn Mater. 2015;395:271–6.

[4] Gaffar SA, Prasad VR, Bég OA. Numerical study of flow and heat transfer of non-Newtonian tangent hyperbolic fluid from a sphere with Biot number effects. Alex Eng J. 2015;54(4):829–41.

[5] Hayat T, Aziz A, Muhammad T, Alsaedi A. Three-dimensional flow of Prandtl fluid with Cattaneo-Christov double diffusion. Results Phys. 2018;9:290–6.

[6] Saleem S, Ahmad B, Naseem A, Riaz MB, Abbas T. Mono and hybrid nanofluid analysis over shrinking surface with thermal radiation: a numerical approach. Case Stud Therm Eng. 2024;54:104023.

[7] Ramana RM, Maheswari C, Shaw SM, Dharmaiah G, Fernandez-Gamiz U, Noeiaghdam S. Numerical investigation of 3-D rotating hybrid nanofluid Forchheimer flow with radiation absorption over a stretching sheet. Results Eng. 2024;22:102019.

[8] Nisar Z, Ahmed B, Aziz A, Muhammad K, Khalifa HAEW, Ahmad I. Mathematical modeling and analysis for radiative MHD peristaltic flow of Bingham nanofluid. ZAMM-J Appl Math Mech/Z Angew Math Mech. 2024;104:e202300840.

[9] Aziz A, Aziz A, Alam MM, Galal AM. Excitation of highly concentrated spoof surface plasmon polaritons based on LC-resonance theory. Eur Phys J Plus. 2023;138(1):61.

[10] Mishra A, Pathak G. A comparative analysis of MoS_2-SiO_2/H_2O hybrid nanofluid and MoS_2-SiO_2-GO/H_2O ternary hybrid nanofluid over an inclined cylinder with heat generation/absorption. Numer Heat Transf Part A: Appl. 2024;85(16):2724–53.

[11] Govind G, Sharma P, Sharma BK, Gandhi R, Almohsen B, Pérez LM. Computational analysis of entropy generation optimization for

Cu–Al2O3 water-based chemically reactive magnetized radiative hybrid nanofluid flow. AIP Adv. 2024;14(7).
[12] Ali A, Hussain S, Ashraf M. Theoretical investigation of unsteady MHD flow of Casson hybrid nanofluid in porous medium: Applications of thermal radiations and nanoparticle. J Radiat Res Appl Sci. 2024;17(3):101029.
[13] Hayat T, Aziz A, Muhammad T, Alsaedi A. Darcy-Forchheimer flow of nanofluid in a rotating frame. Int J Numer Methods Heat Fluid Flow. 2018;28(12):2895–915.
[14] Ogunsola AW, Oyedotun MF. Development of ternary hybrid nanofluid for a viscous Casson fluid flow through an inclined microporous channel with Rosseland nonlinear thermal radiation. Int J Model Simul. 2024;44:1–19.
[15] Paul A, Sarma N, Patgiri B. Numerical assessment of MHD thermomass flow of Casson ternary hybrid nanofluid around an exponentially stretching cylinder. BioNanoScience. 2024;14:1–16.
[16] Rehman A, Khan D, Mahariq I, Elkotb MA, Elnaqeeb T. Viscous dissipation effects on time-dependent MHD Casson nanofluid over stretching surface: A hybrid nanofluid study. J Mol Liq. 2024;408:125370.
[17] Soomro AM, Lund LA, Asghar A, Bonyah E, Shah Z, Garalleh HA. Magnetized Casson SA-hybrid nanofluid flow over a permeable moving surface with stability analysis. Int J Thermofluids. 2024;21:100555.
[18] Ramasekhar G, Mebarek-Oudina F, Suneetha S, Vaidya H, Selvi PD. Computational simulation of Casson hybrid nanofluid flow with Rosseland approximation and uneven heat source/sink. Int J Thermofluids. 2024;24:100893.
[19] Subhani M, Ullah N, Nadeem S, Aziz A, Sardar H. Modeling and numerical analysis of micropolar hybrid-nanofluid flow subject to entropy generation. Int J Mod Phys B. 2024;38(21):2450285.
[20] Aziz A, Aziz A, Ullah I, Muhammad T. An optimal analysis for 3D swirling flow of Jeffrey nanoliquid with Arrhenius activation energy and heat generation/absorption effects. Waves Random Complex Media. 2022;34:1–30.
[21] Aziz A, Aziz A, Ullah I, Shah SI, Mahtab Alam M. Numerical simulation of 3D swirling flow of Maxwell nanomaterial with a binary chemical mechanism and nonlinear thermal radiation effects. Waves Random Complex Media. 2022;32:1–19.
[22] Faltas MS, El-Sapa S. Time-periodic electrokinetic analysis of a micropolar fluid flow through hydrophobic microannulus. Eur Phys J Plus. 2024;139(7):575.
[23] El-Sapa S, Al-Hanaya A. Effects of slippage and permeability of couple stress fluid squeezed between two concentric rotating spheres. Phys Fluids. 2023;35(10):1–28.
[24] Alotaibi MA, El-Sapa S. MHD Couple stress fluid between two concentric spheres with slip regime. Results Eng. 2024;21:101934.
[25] Muthukumar S, Sureshkumar S, El-Sapa S, Chamkha AJ. Impacts of uniform and sinusoidal heating in a nanofluid saturated porous chamber influenced by the thermal radiation and the magnetic field. Numer Heat Transfer Part A: Appl. 2023;84(5):488–506.
[26] Shamshuddin MD, Saeed A, Mishra SR, Katta R, Eid MR. Homotopic simulation of MHD bioconvective flow of water-based hybrid nanofluid over a thermal convective exponential stretching surface. Int J Numer Methods Heat Fluid Flow. 2024;34(1):31–53.
[27] Shamshuddin MD, Gamar F, Ram MS, Salawu SO. Numerical treatment of MHD micropolar nanofluid flow with activation energy, thermal radiation, and Hall current past a porous stretching sheet. Int J Model Simul. 2024;44:1–13.
[28] Hayat T, Kiyani MZ, Alsaedi A, Khan MI, Ahmad I. Mixed convective three-dimensional flow of Williamson nanofluid subject to chemical reaction. Int J Heat Mass Transf. 2018;127:422–9.
[29] Hayat T, Aziz A, Muhammad T, Alsaedi A. Active and passive controls of Jeffrey nanofluid flow over a nonlinear stretching surface. Results Phys. 2017;7:4071–8.
[30] Rana P, Gupta G. Numerical and sensitivity computations of three-dimensional flow and heat transfer of nanoliquid over a wedge using modified Buongiorno model. Comput Math Appl. 2021;101:51–62.
[31] Kudenatti RB, Jyothi B. Computational and asymptotic methods for three-dimensional boundary-layer flow and heat transfer over a wedge. Eng Comput. 2020;36(4):1467–83.
[32] Kudenatti RB, Gogate S SP, Bujurke NM. Asymptotic and numerical solutions of three-dimensional boundary-layer flow past a moving wedge. Math Methods Appl Sci. 2018;41(7):2602–14.
[33] Rana P, Gupta S, Gupta G. FEM computations and Taguchi optimization in nonlinear radiative MHD MWCNT-MgO/EG hybrid nanoliquid flow and heat transfer over a 3D wedge surface. Case Stud Therm Eng. 2023;41:102639.
[34] Oyelakin IS, Lalramneihmawii PC, Mondal S, Sibanda P. Analysis of double-diffusion convection on three-dimensional MHD stagnation point flow of a tangent hyperbolic Casson nanofluid. Int J Ambient Energy. 2022;43(1):1854–65.
[35] Bibi M, Zeeshan A, Malik MY. Numerical analysis of unsteady momentum and heat flow of dusty tangent hyperbolic fluid in three dimensions. Sci Rep. 2022;12(1):16079.
[36] Sohail M, Nazir U, Mukdasai K, Singh M, Singh A, Mohan CR, et al. Transportation of Fe_3O_4-SiO_2-Al_2O_3/EO and SiO_2-Al_2O_3/EO nanoparticles in magnetized Reiner–Philippoff liquid, including modified fluxes *via* Galerkin algorithm: Significance of EMHD. Front Phys. 2023;11:1133550.